Ultrasonics 92 (2019) 8–12

Contents lists available at ScienceDirect

Ultrasonics

journal homepage: www.elsevier.com/locate/ultras

Designing a tunable acoustic resonator based on defect modes, stimulated by selectively biased PZT rods in a 2D phononic crystal

A. Shakeri, S. Darbari*, M.K. Moravvej-Farshi

Nano Plasmophotonic Research Group, Faculty of Electrical and Computer Engineering, Tarbiat Modares University, P.O. Box 14115-146, Tehran 1411713116, Iran

ARTICLE INFO

Keywords:
Phononic crystal
Resonance
Defect
Localized mode

ABSTRACT

Reconfigurable phononic crystals (PnCs) and related devices are highly attractive because of their flexibility for different applications. We present the design procedure for a tunable acoustic resonator based on a 2D PnC, consisting of a periodic array of piezoelectric rods of radii 175 μm as inclusions arranged in air background. A single point defect devised by a rod of radius 161 μm, replacing one of the inclusions, plays the role of the acoustic resonator, leading to a defect frequency in the phononic band gap ($f_d \approx 432$ kHz). Applying a ~1% strain to the defect rod, via an external voltage, tunes the defect resonant frequency within the phononic band gap. It is shown that the maximum tunability and the frequency shift depends on the defect size, and is achieved about $\Delta f_d = 440$ Hz for the defect with the expense of descending quality factor. Considering the pattern of the localized pressure field, we introduce a multi-defect structure with five symmetric defect rods, corresponding to the maxima of field distribution. It is shown that maximum frequency shift of the dominant defect frequency is achieved about $\Delta f_d = 1.14$ kHz for defect radius of 161 μm, when all five defect rods are strained. The proposed tunable filter based on multi-defect structure results in an enhancement of about 2.6 times in the maximum frequency shift, in comparison with the single defect structure, and introduces a promising approach for realizing tunable acoustic devices.

1. Introduction

Phononic crystals (PnCs) are periodic arrays of scatterers in a host medium, creating the phononic band gaps due to Bragg reflections. It is well established that wave propagation in PnCs is influenced by elastic characteristics of both the scatterers and the host medium, including mass density and elastic parameters [1,2]. Adding a defect to a PnC can result in at least an allowed mode within the band gap. Depending on the type of defect, this acoustic mode can be either localized [3] or propagating [4]. Such properties have been widely investigated in order to realize various acoustic devices such as filters [5], waveguides [6,7], lenses [8], and demultiplexers [9].

The opportunity to realize tunable PnCs after manufacturing is highly attractive because of high flexibility and reconfigurability. In this line of research, tunable filters, waveguides or resonators can be implemented and controlled by an external stimulus. There are numerous reports that are based on changing shape or structure of the crystal [10–12], or varying elastic parameters of the applied material [13–19]. Realizing tunable phononic crystal by exerting mechanical stress and deformation can be applicable by physical contact with the crystal and involves external mechanical instrumentations [10–12]. Magnetoelastic coupling is one the latest mechanisms to change the elasticity [13,14], and magnetic permeability tensors and the behavior of the phononic crystal, as a function of the applied external magnetic field. This approach opens up new horizons in the field but suffers from necessity of providing high external magnetic field that enforces high volume and is in contrary to integration goals. Other groups that have worked on changing elasticity have proposed varying temperature or IR-irradiation [15–17], suffering from high power consumption and response time. Among the related reports, there are few works that use piezoelectric materials to tune the PnC behavior by applying an external electric field [18,19]. Electrically controlled piezoelectric PnCs can show fast response and are excellent for dynamic stimulations, while being suitable for integration goals simultaneously.

Here, we propose electrically controlled acoustic resonators, based on defect modes in PnCs. The PnC platform consists of an array of PZT rods in air medium. Applying an external electric voltage to the selective defect rods can lead to the desired tunable defect bands for the structure. For this purpose, we have simulated the presented resonator designs to achieve an optimized tunable resonator.

* Corresponding author.
E-mail address: s.darbari@modares.ac.ir (S. Darbari).

https://doi.org/10.1016/j.ultras.2018.09.001
Received 7 April 2018; Received in revised form 1 September 2018; Accepted 4 September 2018
Available online 05 September 2018
0041-624X/

2. Simulation method

Study of acoustic wave propagation in a periodic medium is based on the equations of motion. In the general case of an arbitrary inhomogeneous elastic medium, the equation of motion for the components of the displacement vector contains both the longitudinal and transverse velocities [20,21]. Here, a 2D PnC, including PZT rods in air background, is studied in which wave propagation is predominant only in the fluid. Since wave in fluid medium, like air, cannot propagate in transverse direction, solid rods can be considered as fluid media with high stiffness and specific mass consequently [8]. Then, the wave equation is simplified as:

$$(C_{11})^{-1}\frac{\partial^2 \mathbf{p}}{\partial t^2} = \nabla\cdot(\rho^{-1}\nabla \mathbf{p}) \tag{1}$$

where $C_{11} = \rho {c_l}^2$ is the longitudinal elastic constant, ρ is the mass density, c_l is the longitudinal velocity, **p** is the acoustic pressure, and ∇ is 2D nabla. We have utilized 2D finite element method (FEM) to solve Eq. (1) numerically, and evaluate acoustic wave propagation, transmission spectra and acoustic pressure field distributions in the investigated PnCs versus plane wave incident acoustic pressures with amplitude of 1 Pa. These simulations have been done by COMSOL Multiphysics software. Transmission spectra of the PnCs are defined as $T = |W_{Out}/W_{In}|^2$, wherein W_{In} and W_{Out} are the incident and output acoustic energies that are achieved by:

$$W_{In} = \int_{SI} \frac{|p|^2}{2\rho c_l} ds, \quad W_{Out} = \int_{S_O} \frac{|p|^2}{2\rho c_l} ds \tag{2}$$

where S_I and S_O are the input and output surfaces of the relating PnC. All boundaries, except input and output ports, are assumed sound hard boundaries with zero normal derivative of the acoustic pressure at that boundary. The input and output ports are assumed radiation boundaries with zero reflection.

To achieve band structure of the PnC we have applied plane wave expansion (PWE) method. Considering the periodicity of the crystal structure, we can apply Bloch theorem and Fourier series [8] of $\rho^{-1}(r)$ and ${C_{11}}^{-1}(r)$, to achieve:

$$[\overline{\rho^{-1}}\ |K+G|^2 - \overline{C_{11}^{-1}}\omega^2]\boldsymbol{p_k}(G') + \sum_{G'\neq G} F(G-G')[\Delta(\rho^{-1})(K+G)\cdot(K+G') - \Delta({C_{11}}^{-1})\omega^2]\boldsymbol{p_k}(G') = 0 \tag{3}$$

where G is the 2D reciprocal lattice vector, K is a 2D Bloch vector, ω is eigenvalue and $\boldsymbol{p_k}(G)$ is eigenvector. Structure factor, F(G), is given for the rods in PnC by [8]:

$$F(G) = \frac{2fJ_1(Gr_0)}{Gr_0} \tag{4}$$

where J_1(x) is the Bessel function of the first kind of order one, $f = \pi\left(\frac{r_0}{a}\right)^2$ is the filling fraction of rods (with radius r_0), and a is the lattice constant in the square lattice. We have solved the eigenvalue equation (Eq. (3)) in order to calculate the band structure of the PnC.

3. Results and discussion

3.1. Tunable resonator based on a single point defect

Fig. 1(a), shows the achieved transmission spectrum of a prefect 11 × 11 phononic crystal. The inset displays the top view scheme of the investigated 2D phononic crystal, which consists of PZT-4D rods standing in air background. The rods have a radius of $r_0 = 175$ μm, while the lattice constant is $a = 490$ μm. The material parameters are $\rho_{air} = 1.2$ kg/m^3, $C_{air} = 343$ m/s, while Poisson ratio (ν) and Young's modulus (E) of PZT are 0.33 and 62 GPa, respectively. It is also notable that the length of PZT rods (L) are assumed very long in comparison with the investigated acoustic wavelength ($L > 10\lambda \approx 1$ cm). To evaluate transmission spectrum of this PnC (according to Eq. (2)), S_I and S_O are assumed the incident and output boundaries as shown by red dashed lines in the inset. Fig. 1(a) reveals that incident frequencies between 224 kHz and 436 kHz are not permitted to transmit the perfect PnC.

Part (b) in this figure displays the band structure of this crystal, which has been achieved by PWE method and illustrates an acoustic band gap between 387 kHz and 433 kHz in this figure. It can be observed that the calculated transmission band gap in part (a) agrees with the band gap in the X direction of band structure in part (b), corresponding to the direction of the incident plane wave (black arrow in the inset of Fig. 1(a)). The inset of Fig. 1(b) manifests the high symmetric points in the first Brillouin zone of the lattice.

Then, we have included a point defect in the middle of PnC and investigated the characteristics. The dimensions (r_0, a) of the defected crystal are the same as the previously investigated perfect crystal, except that the central rod serves as the defect rod with a different radius (r_d) as shown in the inset of Fig. 2(a). Moreover, the inset indicates S_I and S_O by red dashed lines, which are assumed as the incident and the defect boundaries respectively. Fig. 2(a) indicates the achieved resonance spectrum at the point defect of a 11 × 11 PnC, when $r_d = 161$ μm ($r_d < r_0$). Fig. 2(b) illustrates the full range spectrum in logarithmic scale. Red arrows in both parts (a, b) highlight the defect frequency in the band gap.

Fig. 2(c) shows the relating band structure, in which the red-dashed band corresponds to the defect band. This picture was simulated by defining a super-cell, as shown in the inset of part (a), and using PWE method. The nearly flat band nature of the created defect band reveals nearly zero group velocity for the relating acoustic mode. Hence, the created defect mode is expected to be localized and resonating at the defect position. Part (d) in this figure illustrates the pressure field distribution for the defect frequency (f_d), which confirms creation of the localized mode.

It is expected that the defect frequency varies by changing the characteristics of the defect rod in the crystal, such as rod dimension. On the other hand, PZT is a well-known piezoelectric in which external electric field can induce strain and a change in the dimension of the defect rod. Regarding this, we assume an exerted radial strain ($\varepsilon \approx 1\%$) to the defect rod in order to control the defect frequency, and shift the resonance frequency consequently. The proposed structure for the defect rod is depicted as the inset of Fig. 3 schematically, which allows the required radial strain with the minimal internal stress by applying bias voltage (V_{Bias}) to the electrodes. Fig. 3 exhibits the resonance spectrum of the described defective PnC, where the defect peaks before (blue-solid[1] peak) and after (red-dashed peak) exerting strain are magnified. It can be observed that the defect peak shifts to higher frequencies for about 440 Hz, after exerting 1% strain to the defect rod. This reveals a tunability of about +440 Hz for the proposed acoustic resonator, when $r_d/r_0 = 0.92$. It is notable that the required $\Delta r_d \approx 1.6$ μm (equal to $\varepsilon \approx 1\%$) for the defect rod with $r_d/r_0 = 0.92$, can be achieved by applying a bias voltage of about 5 kV to the proposed structure in the inset. It is worth mentioning that we neglected the strain-induced modulation of the defect rod's stiffness because the reported maximum modulation of Young's modulus for $\varepsilon \approx 1\%$ in PZT results in negligible change in the presented transmission and band structure data [22]. This observation is attributed to the inherently extensive difference between the Young's modulus of PZT and air as the background.

Then, we have studied the effect of defect dimension on the strain-induced tunability of the resonance frequency. For this purpose, we simulated single defect structures with different r_d values, and investigated the defect frequency shift (Δf_d) versus exerting $\varepsilon = 1\%$. Fig. 4 indicates the strain-induced Δf_d versus r_d/r_0 (blue-solid curve), when r_d

[1] For interpretation of color in Fig. 3, the reader is referred to the web version of this article.

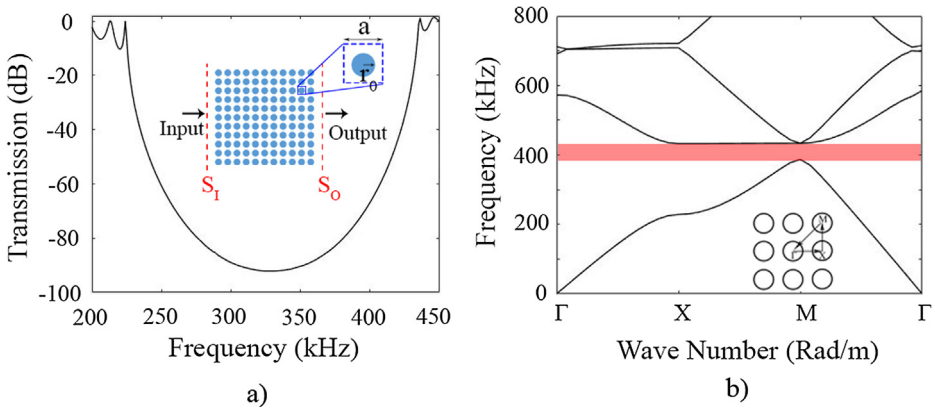

Fig. 1. (a) Transmission spectrum of the investigated PnC. Inset illustrates the top view of the crystal, schematically. (b) Band structure of the investigated PnC.

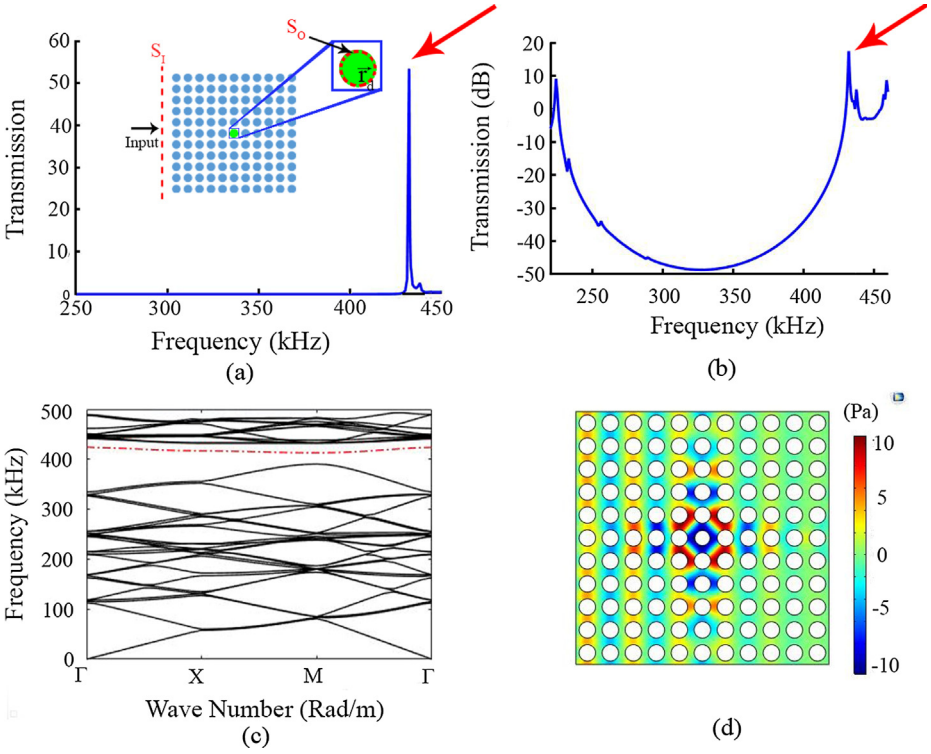

Fig. 2. Resonance spectrum of the single-defect PnC in: (a) linear, and (b) logarithmic scales. Inset in part (a) shows the top view of the PnC, consisting of a single defect as the central rod. (c) Band structure of the defective PnC, where the red-dashed band represents the defect band. (d) Total acoustic pressure field, showing field localization for the defect frequency.

is changed from 70 μm to 270 μm. It is shown that for $r_d < r_0$ blue shift is resulted ($\Delta f_d > 0$), while for $r_d > r_0$ we have red shift of defect frequencies ($\Delta f_d < 0$). It is obvious in this figure that when r_d/r_0 goes to unity, defect frequency in the band gap begins to disappear, and no Δf_d can be defined consequently (shadowed zone). The worthy point here is that the maximum strain-induced frequency shift is achieved $\Delta f_d = +440$ Hz, when $r_d \approx 161$ μm ($r_d/r_0 = 0.92$). However, it should be considered that there is a trade-off between the maximum Δf_d and the quality factor (Q) of the defect peak. It is expected that when r_d/r_0 goes around unity, the crystal resembles a perfect crystal, the defect peak tends to disappear by merging to the pass band, and the quality factor decreases. For clarifying this trade-off, we have superimposed the variation of the quality factor (red-dashed curve) in Fig. 4. It is obviously observable that $r_d/r_0 = 0.61$ is the optimum point, where both Q and Δf_d are maximized simultaneously, for $\varepsilon = 1\%$. This optimum point allows a high quality factor acoustic resonator, with a highly tunable strain-induced resonance frequency.

3.2. Tunable resonator based on a multi-defect structure

At this stage, we have studied a multi-defect PnC with a symmetric defect configuration, which includes 5 defect rods (green rods) at the center of a 11 × 11 crystal, as shown in the inset of Fig. 5(a), schematically. Moreover, the inset indicates S_I and S_O by red lines, which are assumed as the incident and the central defect rod's boundaries (rod No. 3) in the multi-defect configuration. We have chosen this multi-defect structure in correspondence with the pattern of the field distribution relating to the discussed single defect structure. In other words, the defect rods are selected at the positions of pressure field maxima in Fig. 2(d). Hence, we expect that this structure shows significant sensitivity to the equal exerted strain, and an improved tunability can be obtained consequently. It should be noted that we have studied tunability of the described multi-defect structure for both (*i*) $r_d \approx 161$ μm ($r_d/r_0 = 0.92$), and (*ii*) $r_d \approx 106.75$ μm ($r_d/r_0 = 0.61$). According to the aforementioned discussion on the single defect structure in Fig. 4, the first case corresponds to the achievable maximum frequency shift, while the second case relates to the optimized point where both frequency shift and quality factor values are

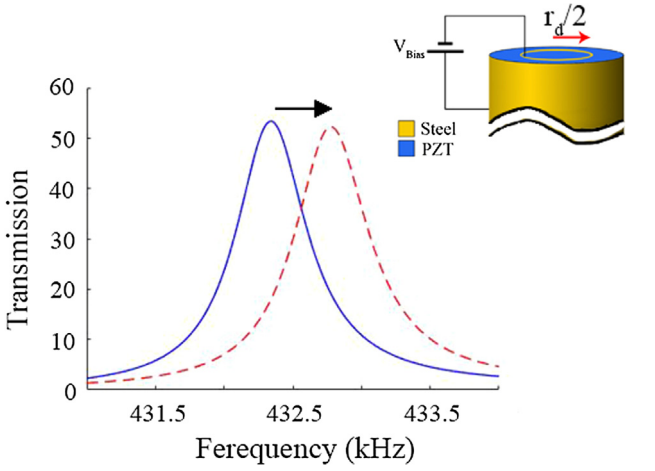

Fig. 3. Resonance spectrum of the single defect structure (with $r_d/r_0 = 0.92$) shifts to higher frequencies for about 440 Hz, by exerting 1% strain to the defect rod. The inset shows the proposed structure for exerting strain to the defect rod schematically.

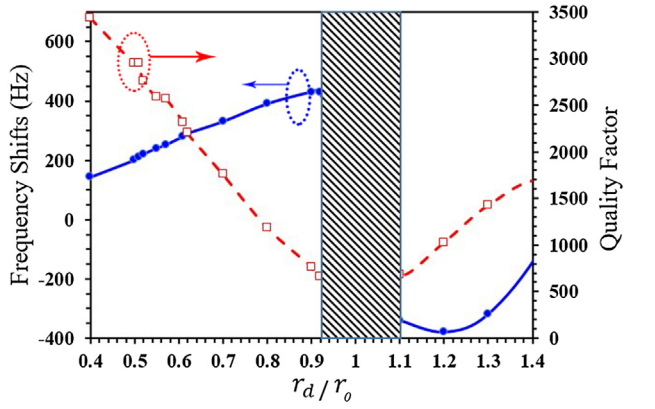

Fig. 4. Variation of Δf_d (solid-blue curve) and Q (dashed-red curve) for the defect band, versus r_d/r_0, for $\varepsilon = 1\%$.(For interpretation of the references to colour in this figure legend, the reader is referred to the web version of this article.)

maximized simultaneously. The other structural parameters are the same as the previous part, for single defect. Parts (a) and (b) of Fig. 5 display the resonance spectrum of the investigated multi-defect crystal with $r_d/r_0 = 0.61$ in linear and logarithmic scales respectively, where two defect bands in the band gap are shown by red arrows.

Part (c) shows the pressure field distribution for $f_{d1} = 426.14$ kHz, the symmetric defect mode, which reveals similar distribution pattern to the investigated single defect structure, but stronger localization around the defect sites (as compared with Fig. 2(c)). Fig. 5(d), also depicts the non-symmetric pressure distribution for the second defect ($f_{d2} = 433.13$ kHz).

Now, we study different configurations to exert strain to the proposed multi-defect structure. For this purpose, we have applied strain to one of the defect rods, then two, three, four and all five defect rods, subsequently (see parts (a) to (i) in Table 1). The first row displays the cropped view of the investigated 11 × 11 defected PnC around the multi-defect structure, where green rods are the relaxed defect rods, and red rods are the stimulated defect rods with $\varepsilon = 1\%$ in each configuration. Blue rows in Table 1 summarize the Δf_d and Q results for each investigated configuration, when $r_d/r_0 = 0.92$. Green rows present the similar results for the optimized dimension, when $r_d/r_0 = 0.61$. It is notable that the tabulated results are related to the first symmetric defect band ($f_d = 426.14$ kHz) of the investigated multi-defect structure.

First, we consider the strained configuration (a), where rod No. 1 (Fig. 5(a)) is strained. It should be noted that exerting strain to rod numbers 1, 2, 4 and 5 lead to nearly the same frequency shifts, due to symmetry of the investigated multi-defect structure. Configuration (b), corresponding to the case when strain is applied to defect rod No. 3, leads to a higher frequency shift in comparison with the previous configuration. The next two configurations are related to the cases when strain is applied to two of the defect rods, which are highlighted by red rods in configurations (c) and (d) in Table 1. The tabulated results show higher frequency shifts in these latter two cases in comparison with previous ones, due to controlling more sensitive sites of the multi-defect structure. As expected, the behavior of the multi-defect structure is sensitive to the sites where pressure field is localized (sites 1–5 in Fig. 5(a)). Similarly, configurations with three and four strained defect rods indicate enhanced frequency shifts, respectively (configurations (e)–(h) in Table 1). Finally, the configuration with 5 strained defect rods is illustrated as configuration (i) of Table 1, which has resulted in the highest frequency shift. In other words, when all the defective and sensitive sites are strained a considerable frequency shift is achieved, which is enhanced by a factor of about 2.63, comparing with the single defect structure (Fig. 3). The proposed tunable acoustic resonator is promising for different application fields such as reconfigurable sensors and filters for sound navigation and ranging (SONAR) techniques, or energy harvesting. Among these potential applications, energy harvesting from ultrasonic sources for implantable biomedical devices is an attractive candidate for our proposed resonator. The proposed structure seems especially promising for the biomedical devices with high cost or high risk accessibility. In this regard, we can refer to a report on microfabricated PZT diaphragm array, which has been utilized to realize self-powered biomedical devices that harvest energy of the incident ultrasonic wave [23]. Their structure suffer from low efficiency energy conversion, which can be overcome by the ability of wave localization in our proposed miniature PnC structure. For this purpose, energy harvester can be embedded in the designed PnC-based cavity, so that the resonance frequency of the micro-harvester is matched with the resonance frequency of our acoustic resonator [24]. Moreover, the filtering behavior of the surrounding PnC can prevent the harvester from being influenced by any other undesired environmental wave with forbidden frequency.

4. Conclusion

Here, tunable acoustic resonators have been introduced and investigated, based on defect sites in PnC. The proposed phononic crystal consists of PZT rods standing in air medium, while defect rods are assumed by the same material but different radii. Defect rods lead to defect bands in the band gap, which depend on the dimension and structure of the defect. Regarding the piezoelectric property of PZT, electrically controlled radial strain can be exerted to the defect rods that lead to tunable defect bands, or resonance frequency. Considering the pattern of the localized pressure field, we introduced single defect and multi-defect structures, and demonstrated that the maximum frequency shift is enhanced by a factor of about 2.63 for the multi-defect structure. Moreover, we have optimized the size and the strain configuration to compromise between the frequency shift and quality factor of the defect band. The proposed reconfigurable resonator is highly attractive because of its operational flexibility after manufacturing, and can lead to emerging new generations of tunable devices such as sensors, filters and energy harvesting applications.

Acknowledgments

The authors acknowledge the partial financial support of the Iran National Science Foundation (INSF), and the financial support from Tarbait Modares University, through grant #IG-39703.

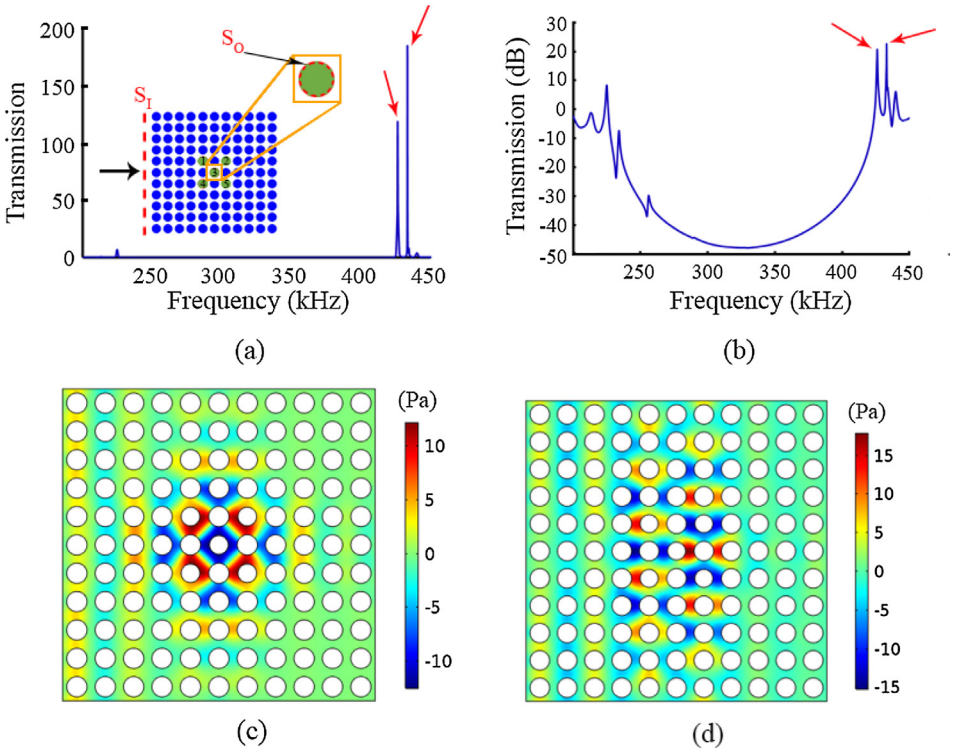

Fig. 5. The resonance spectrum of the multi-defect structure with two defect bands in: (a) linear, and (b) logarithmic scales. The inset of part (a) shows the top view of the investigated multi-defect PnC, where green rods present the defect rods with $r_d/r_0 = 0.92$. (c), (d) Pressure distribution patterns of the lower and higher defect frequencies, respectively.

Table 1
The achieved Δf_d and Q results for different strained configurations of the multi-defect structure. First row illustrates the cropped view of the investigated 11 × 11 defected PnC, where red rods represent the strained defect rods with $\varepsilon = 1\%$, and green rods show the relaxed defect rods. Blue rows correspond to $r_d/r_0 = 0.92$, while green rows are related to $r_d/r_0 = 0.61$.

Strained Config.									
	(a)	(b)	(c)	(d)	(e)	(f)	(g)	(h)	(i)
Δf_d (Hz)	180	390	360	370	550	750	760	740	1140
Q	1152.2	1122.5	1152.8	1152.8	1122.9	1094.7	1094.6	1123.4	1042.8
Δf_d (Hz)	70	170	140	140	210	320	320	290	460
	5636.7	4930.4	5634.3	4930	5635.4	5636.9	5636.9	5636.4	5638.9

References

[1] M. Si galas, E.N. Economou, Band structure of elastic waves in two dimensional systems, Solid State Commun. 86 (1993) 141–143.
[2] M.S. Kushwaha, P. Halevi, L. Dobrzynski, B. Djafari-Rouhani, Acoustic band structure of periodic elastic composites, Phys. Rev. Lett. 71 (1993) 2022–2025.
[3] R.H. Olsson III, I.F. El-Kady, M.F. Su, M.R. Tuck, J.G. Fleming, Microfabricated VHF acoustic crystals and waveguides, Sens. Actuat. 145 (2008) 87–93.
[4] H. Zhu, F. Semperlotti, Metamaterial based embedded acoustic filters for structural applications, AIP Adv. 3 (2013) 092121.
[5] A. Khelif, B. Djafari-Rouhani, J. Vesseur, P. Deymier, P. Lambin, L. Dobrzynski, Transmittivity through straight and stublike waveguides in a two-dimensional phononic crystal, Phys. Rev. B 65 (2002) 174308.
[6] T. Miyashita, C. Inoue, Numerical investigations of transmission and waveguide properties of sonic crystals by finite-difference time-domain method, Jpn. J. Appl. Phys. 40 (2001) 3488–3492.
[7] H. Chandra, P.A. Deymier, J.O. Vasseur, Elastic wave propagation along waveguides in three-dimensional phononic crystals, Phys. Rev. B 70 (2004) 054302.
[8] R.H. Olsson III, I. El-Kady, Microfabricated phononic crystal devices and applications, Meas. Sci. Technol. 20 (2008) 012002.
[9] Y. Pennec, B. Djafari-Rouhani, J.O. Vasseur, A. Khelif, P.A. Deymier, Tunable filtering and demultiplexing in phononic crystals with hollow cylinders, Phys. Rev. E 69 (2004) 046608.
[10] S. Hedayatrasa, K. Abhary, M.S. Uddin, J.K. Guest, Optimal design of tunable phononic bandgap plates under equibiaxial stretch, Smart Mater. Struct. 25 (2016) 055025.
[11] A. Bayat, F. Gordaninejad, Dynamic response of a tunable phononic crystal under applied mechanical and magnetic loadings, Smart Mater. Struct. 24 (2015) 065027.
[12] J. Shim, P. Wangb, K. Bertoldi, Arnessing instability-induced pattern transformation to design tunable phononic crystals, Int. J. Solids Struct. 58 (2015) 52–61.
[13] O. Bou Matar, J.F. Robillard, J.O. Vasseur, A.-C. Hladky-Hennion, P.A. Deymier, P. Pernod, V. Preobrazhensky, Band gap tunability of magneto-elastic phononic crystal, J. Appl. Phys. 111 (2012) 054901.
[14] C. Gu, F. Jin, Research on the tunability of point defect modes in a two-dimensional magneto-elastic phononic crystal, J Phys. D 49 (2016) 175103.
[15] B. Rostami-Dogolsara, M.K. Moravvej-Farshi, F. Nazari, Acoustic add-drop filters based on phononic crystal ring resonators, Phys. Rev. B 93 (2016) 014304(6).
[16] B. Rostami-Dogolsara, M.K. Moravvej-Farshi, F. Nazari, Designing switchable phononic crystal-based acoustic demultiplexer, IEEE Trans. Ultrason. Ferroelectr. Freq. Control 63 (2016) 1468–1473.
[17] E. Walker, D. Reyes, M.M. Rojas, A. Krokhin, Z. Wang, A. Neogi, Tunable ultrasonic phononic crystal controlled by infrared radiation, Appl. Phys. Lett. 105 (2014) 143503.
[18] C. Croenne, M.-F. Ponge, B. Dubus, C. Granger, Tunable phononic crystals based on piezoelectric composites with 1–3 connectivity, J. Acoust. Soc. Am. 139 (2016) 3296.
[19] S.L. Vatanabe, G.H. Paulino, Silva, Maximizing phononic band gaps in piezocomposite materials by means of topology optimization, J. Acoust. Soc. Am. 136 (2014) 494–501.
[20] A. Khelif, A. Adibi, Phononic Crystals Fundamentals and Applications, Springer, New York, 2016.
[21] M. Kushwaha, P. Halevi, Giant acoustic stop bands in two-dimensional periodic arrays of liquid cylinders, Appl. Phys. Lett. 69 (1996) 31–33.
[22] T. Fett, S. Mueller, D. Munz, G. Thun, Nonsymmetry in the deformation behaviour of PZT, J. Mater. Sci. Lett. 17 (1998) 261–265.
[23] Q. Shi, T. Wang, C. Lee, MEMS based broadband piezoelectric ultrasonic energy harvester (PUEH) for enabling self-powered implantable biomedical devices, Sci. Rep. 6 (2016) 24946.
[24] M. Javadi, A. Heidari, S. Darbari, Realization of enhanced sound-driven CNT-based triboelectric nanogenerator, utilizing sonic array configuration, Curr. Appl. Phys. 18 (4) (2018) 361–368.